Pure appl. geophys. 159 (2002) 1447–1464
0033–4553/02/081447–18 $ 1.50 + 0.20/0

Pure and Applied Geophysics

Synthetic Seismograms and Wide-angle Seismic Attributes from the Gaussian Beam and Reflectivity Methods for Models with Interfaces and Velocity Gradients

ROBERT L. NOWACK[1] and STEPHEN M. STACY[1]

Abstract — The effects of interfaces and velocity gradients on wide-angle seismic attributes are investigated using synthetic seismograms. The seismic attributes considered include envelope amplitude, pulse instantaneous frequency, and arrival time of selected phases. For models with interfaces and homogeneous layers, head waves can propagate which have lower amplitudes, as well as frequency content, compared to the direct arrivals. For media with interfaces and velocity gradients, higher amplitude diving waves and interference waves can also occur. The Gaussian beam and reflectivity methods are used to compute synthetic seismograms for simple models with interfaces and gradients. From the results of these methods, seismic attributes are obtained and compared. It was found that both methods were able to simulate wide-angle seismic attributes for the simple models considered. The advantage of using the Gaussian beam method for seismic modeling and inversion is that it is fast and also asymptotically valid for laterally varying media.

Key words: Wide-angle seismic attributes, synthetic seismograms, seismic refraction.

Introduction

In this paper synthetic seismograms are used to investigate the effects of interfaces and velocity gradients on wide-angle seismic attributes. The seismic attributes considered include envelope amplitude, pulse instantaneous frequency, as well as arrival time of selected phases. These attributes can be used for seismic inversion for elastic and anelastic structure and provide an alternative to more complete wavefield inversions. For example, NOWACK and MATHENEY (1997a) and MATHENEY *et al.* (1997) performed inversions using observed seismic attributes for smoothly varying upper crustal structure.

One of the important aspects of seismology is the interplay between smoothly varying media and interfaces in the earth. Although many material discontinuities occur in the earth, smoothly varying, homogenized earth models separated by a relatively small number of interfaces can often be used. Here we will investigate the

[1] Department of Earth and Atmospheric Sciences, Purdue University, West Lafayette, IN 47907. E-mail: nowack@purdue.edu

effects of large contrast interfaces on wide-angle seismic attributes. For models with interfaces between homogeneous layers, head waves can propagate which have lower amplitudes, as well as frequency content, compared to direct arrivals. However, higher amplitude refracted waves are often observed resulting from velocity gradients. For these types of media, a number of body-wave phases can propagate including diving waves, reflected waves, and interference waves.

The Gaussian beam and reflectivity methods are used to compute synthetic seismograms in simple models with interfaces and velocity gradients, and from these, seismic attributes are obtained and compared. The reflectivity method is a full-wave method which assumes layered earth models. The Gaussian beam method is an asymptotic method for high-frequency seismic waves. The method is valid at caustics, and when wide beam parameters are used, can simulate head-wave phases. With a careful selection of parameters, both methods were found to be able to simulate seismic attributes for the models considered. The Gaussian beam method has the advantage of being fast, as well as being asymptotically valid in laterally varying media.

Refraction effects on seismic attributes

The first example we investigate is for a layer over a half-space for which a head wave can propagate. For this case, if the direct wave has a spectrum of $S(\omega)$, then the head-wave branch will have a spectrum proportional to $(i/\omega)S(\omega)$ (AKI and RICHARDS, 1980). In the time-domain, this corresponds to a smoother, integrated waveform compared to the direct arrival. Using seismic attributes derived from synthetic seismograms, NOWACK and MATHENEY (1997b) found that the time-domain instantaneous frequency of the pure head wave is also lowered with respect to the direct wave. For distances greater than the critical distance, the head-wave amplitude decays as $r^{-1/2}L^{-3/2}$ where r is the distance and L is the distance traveled in the lower medium. For distances much greater than the interface depth, the head-wave amplitude approximately decays as r^{-2} which is lower than that of the direct wave amplitude.

Figure 1 illustrates the effects of a layer over a half-space on the frequency content of the first arrivals. Figure 1A shows a velocity model with an interface at 25 km with a velocity contrast from 6 to 8 km/s. Synthetic seismograms for this model were computed using the reflectivity method (FUCHS and MÜLLER, 1971; KIND, 1978; MÜLLER, 1985). Two models are considered: first a model with low attenuation ($Q = 2000$), and then a model with a constant Q of 150. Figure 1B depicts the pulse instantaneous frequencies obtained using the method of MATHENEY and NOWACK (1995) for the low attenuation case (squares) and the $Q = 150$ case (triangles). The gap in distance near 130 km is where the attributes are not computed due to interference near the cross-over distance. The refracted arrivals occur for

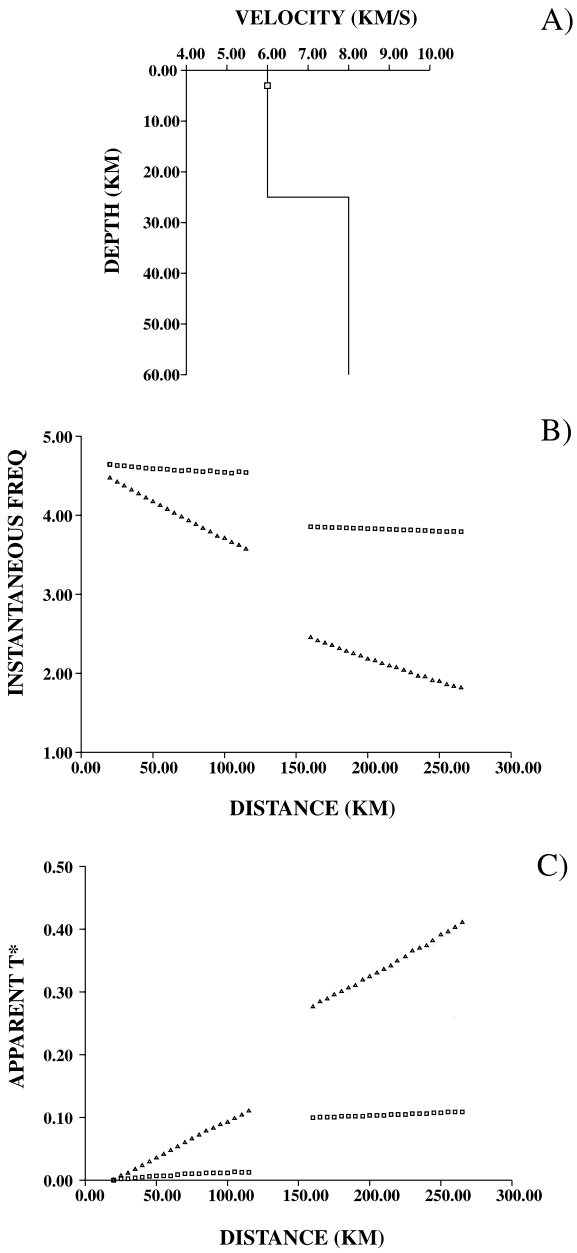

Figure 1

A) A layer over a half-space with an interface at 25 km and a velocity increase from 6 to 8 km/s. B) The computed pulse instantaneous frequencies for the first arrivals for a low attenuation case (squares) and a $Q = 150$ case (triangles). The gap in distance is near the cross-over distance for the branches where attributes for the crossing phases were not computed. C) The apparent t^* values from the instantaneous frequencies in B) are shown using the matching method of MATHENEY and NOWACK (1995).

distances exceeding this distance. For the low attenuation case, the refracted pulse frequency lowers as a result of the head wave in comparison to the direct wave. A similar frequency effect is seen for the $Q = 150$ case.

Using the instantaneous frequency matching method of MATHENEY and NOWACK (1995), apparent t^* values can be estimated, and are shown in Figure 1C for a source pulse with a center frequency of 4.77 Hz. For the low attenuation case (squares) there is a step increase in the apparent t^* values of about 0.1 between the direct and refracted arrivals. For the $Q = 150$ case, the apparent t^* values increase linearly with distance related to the attenuation model. There is also a step increase between the direct and refracted arrivals which would increase the apparent t^* estimate by about 38% at a distance of 150 km. An average Q can be inferred from the travel-time divided by t^*, and at this distance would give a biased Q value.

For a model with two layers over a half-space, the first arrivals consist of a direct wave and two head-wave phases, one for each interface. If the reference pulse is taken along a refracted phase for a shallow interface, then seismic attributes extracted for the two refracted arrivals will have the same frequency characteristics. Thus frequency attributes at the cross-over distance of the branches between a shallow and deeper interface will have no further lowering in frequency. If an attenuation model is included, there would now be continuity of the changing frequency characteristics between the two refraction branches (NOWACK and MATHENEY, 1997b). However, there would still be changes between the direct wave and the refracted branches.

An example of a model with two nearly homogeneous crustal layers and an upper mantle lid is given by IASP91 in Figure 2A (KENNETT and ENGDAHL, 1991). Even considering a spherical earth correction, the gradients for this model are relatively low, and head-wave effects can occur.

The previous examples were for simple cases of interfaces between nearly homogeneous layers. For models with interfaces and velocity gradients, a number of waves can propagate which can have effects on the first-arrival seismic attributes (ČERVENÝ and RAVINDRA, 1971; HILL, 1971). Positive gradients will result in diving and interference waves. Negative velocity gradients will result in reduced amplitude diffracted waves (ČERVENÝ and RAVINDRA, 1971). Curvature of boundaries will also result in interference or diffracted head waves (HILL, 1973). Refracted wave amplitudes from observed crustal data have supported the interpretation that refracted arrivals are often in the form of diving or interference waves instead of pure head waves, with similar travel times but different secondary attributes (BRAILE and SMITH, 1975).

HILL (1971) showed that by using the amplitudes of the refracted wave phases, the effects of velocity and attenuation structure cannot be easily separated. BRAILE (1977), however, inferred by reflectivity modeling that the use of travel times and amplitudes of crustal phases, in addition to P_n phases, allows for some resolution of velocity and attenuation structure for models with interfaces. Nonetheless, even in

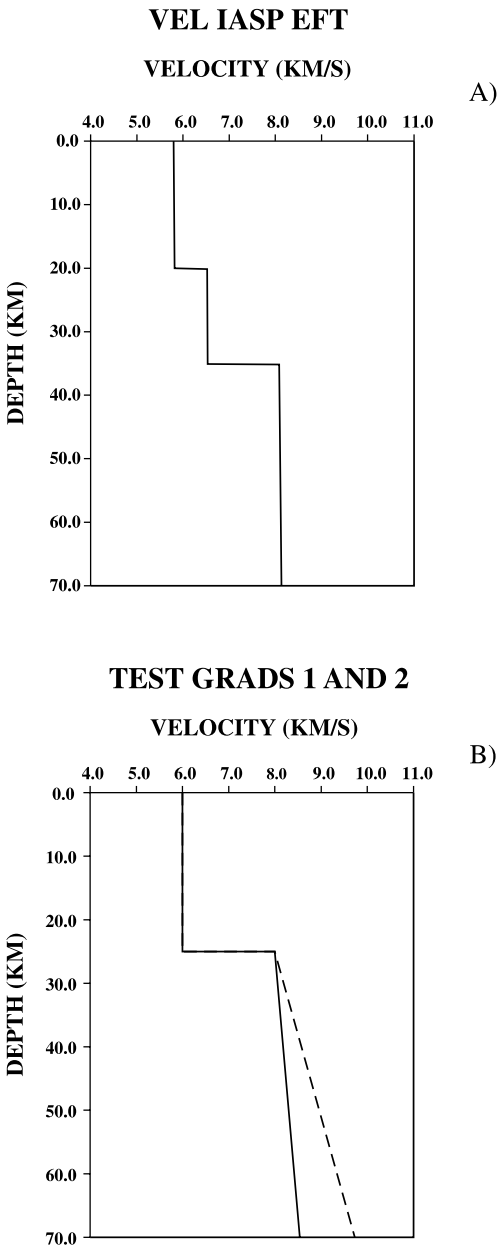

Figure 2
A) The velocity model IASP91 showing the crust and upper mantle lid (KENNETT and ENGDAHL; 1991). B) Velocity models 1 and 2 with two different velocity gradients below an interface (solid and dashed lines, respectively).

spherically symmetric earth models, attenuation estimates using P_n can be biased by refraction effects (SERENO and GIVEN, 1990).

Here we will investigate refraction effects on seismic attributes using simple models with velocity gradients below an interface, which will result in diving and interference waves. Positive effective gradients can also be obtained by flattening a spherical earth model (AKI and RICHARDS, 1980). We compute synthetic seismograms using both the reflectivity method (FUCHS and MÜLLER, 1971; KIND, 1978; MÜLLER, 1985; RUDMAN *et al.*, 1993) and the Gaussian beam method (POPOV, 1982; ČERVENÝ *et al.*, 1982; ČERVENÝ, 1985). Secondary seismic attributes, including amplitude and instantaneous frequency, are then computed and compared.

An example of a partial ray expansion for an interference refracted wave is given in Figure 3. In Figure 3A a velocity model with a positive velocity gradient below an interface is shown. Figures 3B, 3C and 3D show the diving ray as well as the first and second subinterface multiples out to regional distances. Although refracted waves are often modeled for travel times using diving rays, for a significant distance range an interference wave can exist which will affect the characteristics of the secondary attributes. ČERVENÝ and RAVINDRA (1971) gave approximate expressions for the interference refracted waves, and also at what distances successive waves separate from the interference wave. The separation of individual phases depends on the velocity gradient, as well as the pulse frequency. Finite frequency interference effects were studied by CORMIER and RICHARDS (1977) for the inner core boundary using a full wave theory based on a complete expansion of the interference waves. A comparison between this full wave theory with the reflectivity method was then performed by CHOY *et al.* (1980). Here we compare the results of a partial expansion of interface waves using the Gaussian beam method with the reflectivity method, and also compare the derived secondary seismic attributes.

Figure 2B shows two velocity models with velocity gradients below an interface. In each model, the interface is at 25 km with a velocity changing from 6 to 8 km/s. An explosive source is located at 6 km. In model 1, the velocity gradient goes from 8 km/s below the interface to 8.18 km/s at a depth of 40 km. In model 2, a steeper velocity gradient is used going from 8 km/s below the interface to 8.57 km/s at a depth of 40 km. The velocity gradient then continues linearly to greater depths, depending on the model.

Using the reflectivity method, synthetic seismograms were computed using two algorithms, the modified reflectivity method of KIND (1978) and the reflectivity algorithm given by RUDMAN *et al.* (1993). Both algorithms were found to be sensitive to the layer thickness used to approximate the velocity gradient. With the integration parameters used, the algorithm of RUDMAN *et al.* (1993) was found to be more time consuming but gave somewhat better results for the direct and reflected phases in the upper homogeneous layer. The reflectivity synthetics shown in Figures 4 and 5 were obtained using the algorithm described by RUDMAN *et al.* (1993). For the reflectivity synthetics using model 1, a layer thickness of 0.1875 km

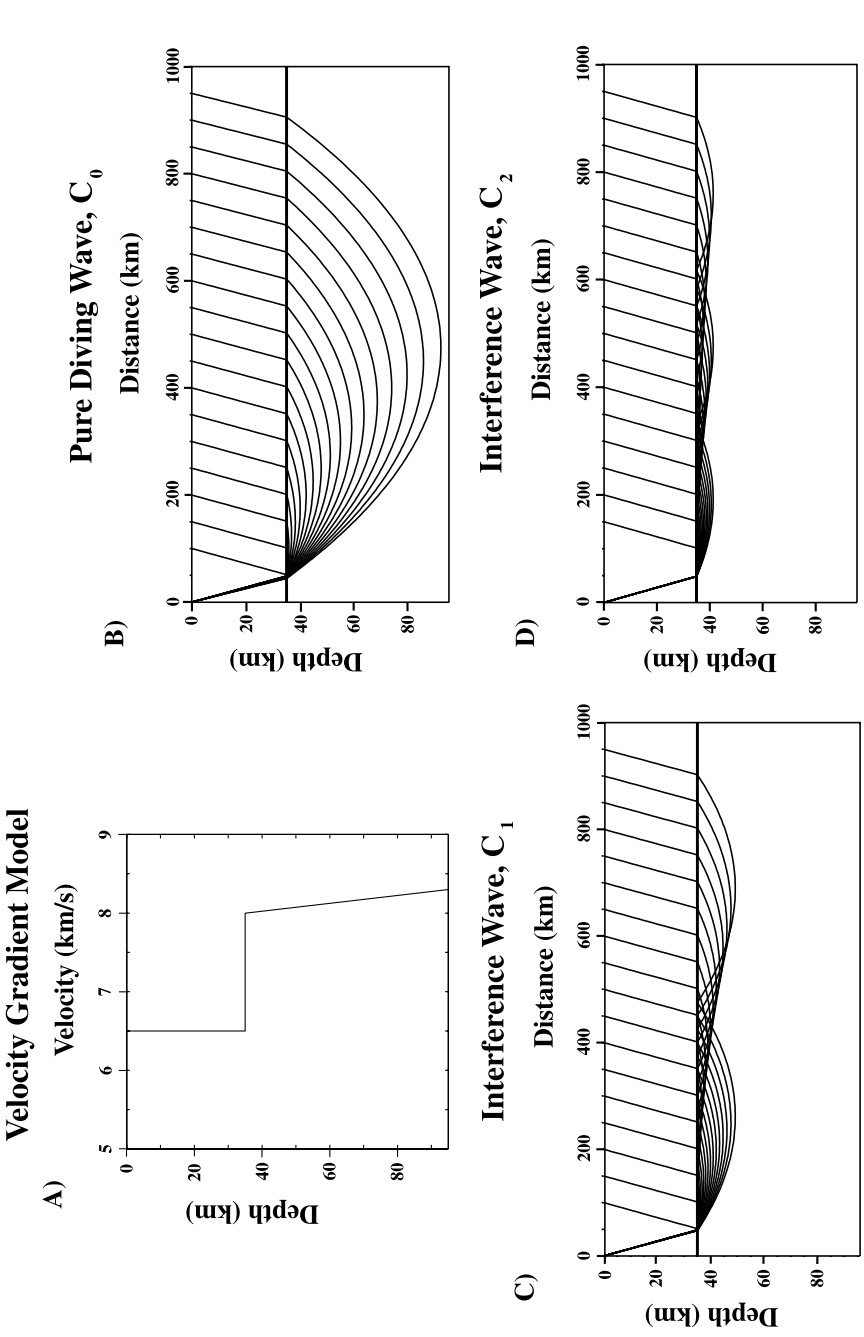

Figure 3
An example of several rays of a partial ray expansion for the interference wave out to regional distances for a positive velocity gradient below an interface. A) A velocity model showing a linear velocity gradient below an interface. B) shows the diving ray, C) the first subinterface multiple, and D) the second subinterface multiple.

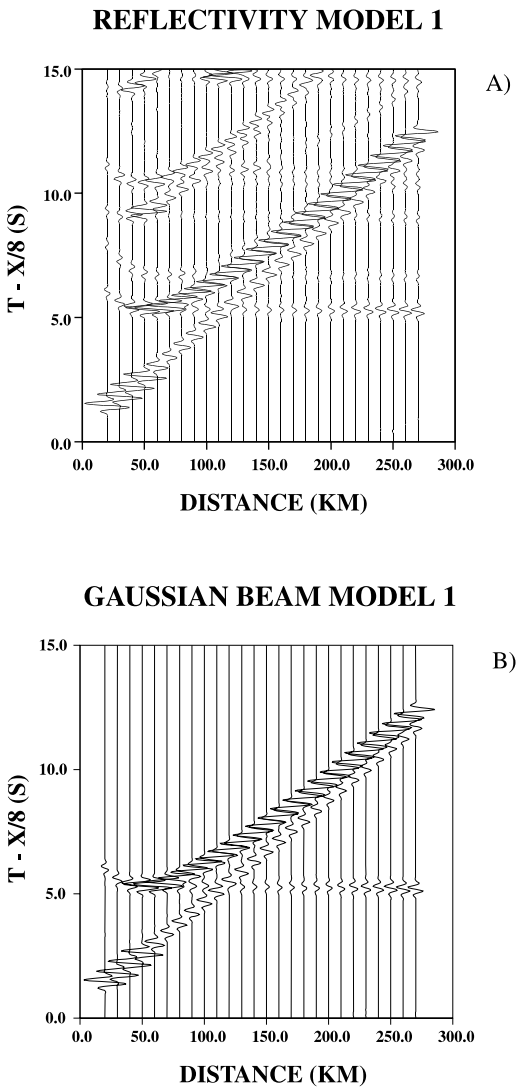

Figure 4
Synthetic seismograms and derived seismic attributes for model 1 shown in Figure 2. A) Synthetic seismograms using the reflectivity method. B) Synthetic seismograms using the Gaussian beam method. C) Envelope amplitudes of the first arrivals obtained from reflectivity modeling (squares) and Gaussian beam modeling (plus signs). D) Instantaneous frequencies for first arrivals obtained from reflectivity modeling (squares) and Gaussian beam modeling (plus signs).

was used to approximate the velocity gradient down to 55 km. In Figure 4D, a finer layer thickness of 0.1 km and the double precision algorithm of KIND (1978) were used for the comparison of the pulse instantaneous frequencies. For model 2, a layer

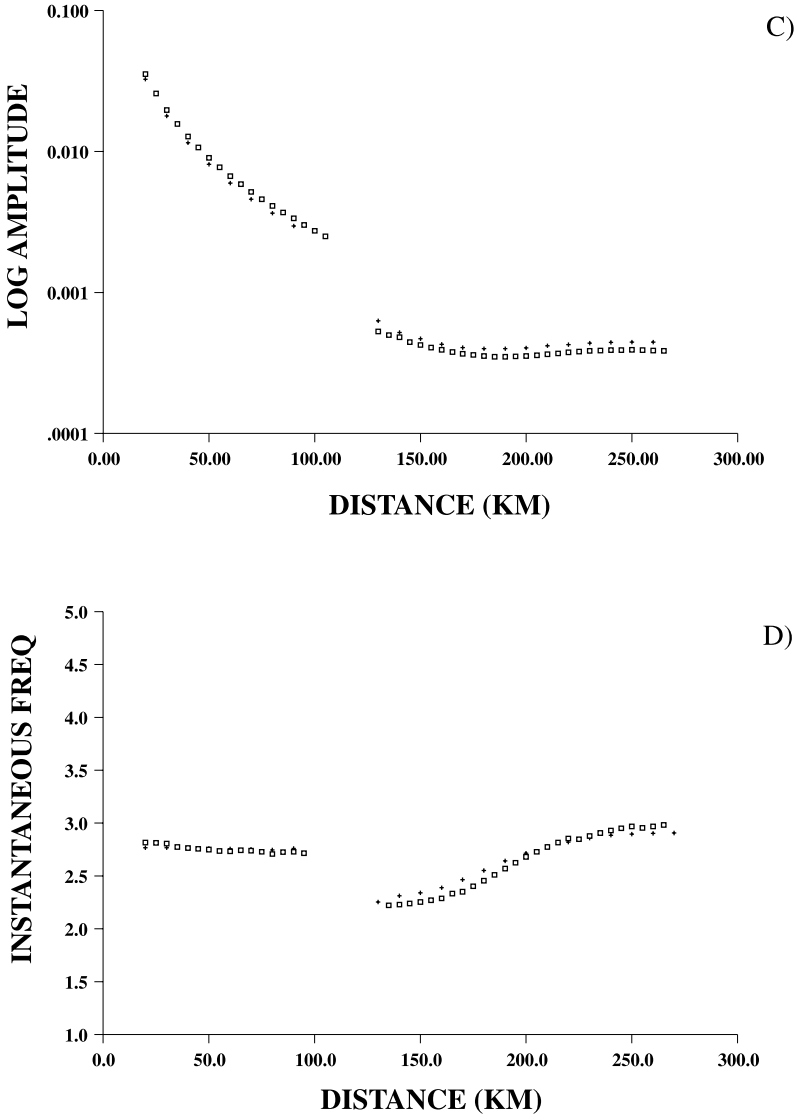

Figure 4C,D

thickness of 0.34375 km was used to a depth of 80 km, since for this case the diving ray penetrates to greater depths. The reflectivity synthetics were then used to compute secondary seismic attributes which are compared with the results from the Gaussian beam method.

The Gaussian beam method is an asymptotic method for the computation of high frequency seismic waves, and was proposed by POPOV (1982) and initially applied by

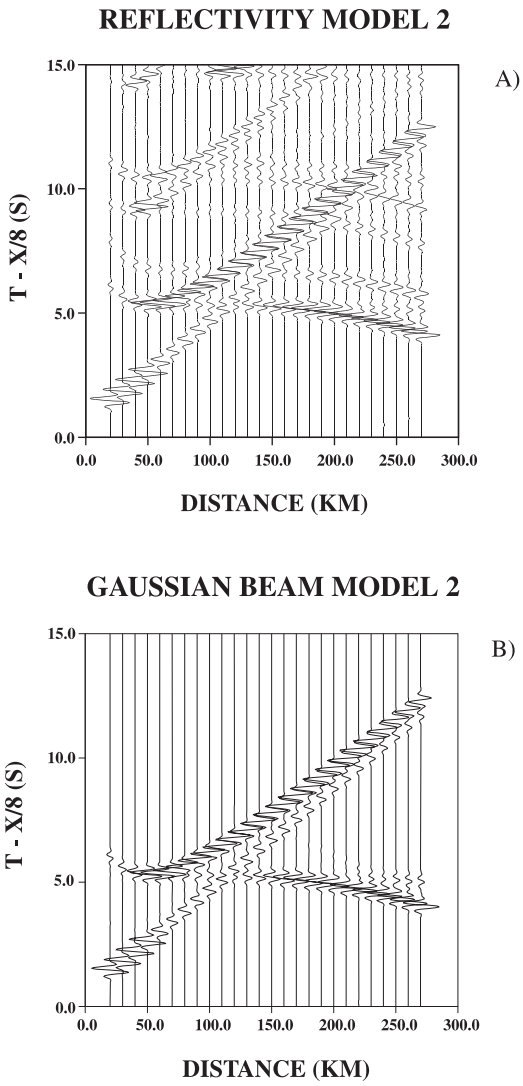

Figure 5
Synthetic seismograms and derived seismic attributes for model 2 shown in Figure 2. A) Synthetic seismograms using the reflectivity method. B) Synthetic seismograms using the Gaussian beam method. C) Envelope amplitudes of the first arrivals obtained from reflectivity modeling (squares) and Gaussian beam modeling (plus signs). D) Instantaneous frequencies for first arrivals obtained from reflectivity modeling (squares) and Gaussian beam modeling (plus signs).

Červený *et al.* (1982). It has an advantage over the standard ray method of providing finite results at caustics. The method involves the summation of individual paraxial Gaussian beams along ray trajectories as

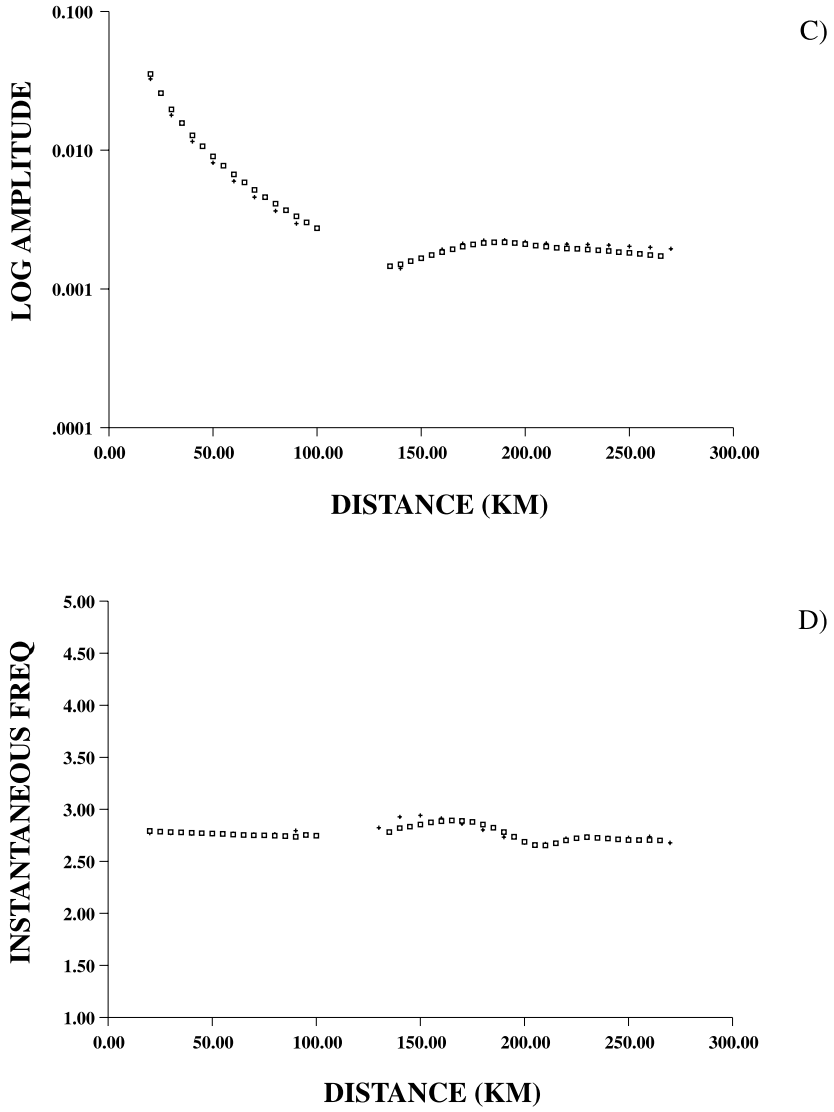

Figure 5C,D

$$\vec{u}(\vec{x},\omega) = \iint_D \Phi(\gamma_I)\vec{u}^{GB}_{\gamma_I}(\vec{x},\omega,M(s_b))\,d^2\gamma \ ,$$

where $\vec{u}^{GB}_{\gamma_I}$ are the individual beam solutions, $\Phi(\gamma_I)$ are the weighting functions, and $M(s_b)$ are the beam parameters for a specified position s_b along the ray. The ray parameters γ_I $(I = 1, 2)$ are used to specify the central ray for each beam along the

initial wavefront, and the domain D depends on the type of source to be decomposed into beams. A review of the Gaussian beam method is given by ČERVENÝ (1985), and a recent overview is presented by NOWACK (2002).

For the case of the interference wave, the specification of beam parameters is complicated by different requirements of the solution. For the wide-angle reflected phase, broad beams are required to accurately represent the head-wave component of the solution (NOWACK and AKI, 1984). However, for multiple underside reflections, both caustics, as well as pseudo-caustics of individual plane wave components, can result and finite sized beams are required to ensure nonsingular solutions. For both the reflected waves and the multiply reflected underside reflections, the beams are specified by effective plane waves at the receiver which provide stable summations. In addition, the imaginary parts of the complex curvatures must be specified and we have used a semi-automatic expansion resulting in broad beams that also limit discretization error. ČERVENÝ (1985) noted that this choice produces better results for vertically varying media. However, for the wide-angle reflections, somewhat broader beams were used to ensure that the head-wave contribution was obtained. Finally, the Gaussian beam method was run in ray mode for the direct wave since this wave is regular. The resulting Gaussian beam solution is then obtained as a combination of the individual wave components.

The reflectivity seismograms for model 1 are shown in Figure 4A, and the seismograms using the Gaussian beam method are shown in Figure 4B. The source pulse was given by a Gabor wavelet with a dominant frequency of 2.77 Hz and a gamma value of 3.75 which specifies the width of the spectral envelope. The Gaussian beam calculations include only the direct arrival, the wide-angle reflection and the interference wave made of up to 8 underside reflections. The wide beam parameters used for the wide-angle reflections also allow for a head wave contribution. The reflectivity method, in contrast, computes the complete wavefield. In addition to the direct, reflected and refracted P-waves, the results also include surface reflected and later arrivals. For the direct and wide-angle P-wave arrivals, a good agreement between the two methods was found. For the first arrivals, the pulses initially broaden after the cross-over distance decreases the frequency, and then slowly increase in frequency (Figures 4A and 4B). However, the diving wave does not separate from the interference waves for these distances.

The results for model 2 are shown in Figure 5 where the reflectivity results are given in Figure 5A and the Gaussian beam results in Figure 5B. For this model, the diving wave separates from the interference wave at about 220 km. For greater distances, the first arrival is the diving wave which is a geometric arrival. The separation distances for multiply reflected underside reflections from the interference wave package are given by ČERVENÝ and RAVINDRA (1971). Although a greater layer thickness was used for the reflectivity modeling in this case because of the greater penetration of the diving wave, there is still a good agreement between the reflectivity and Gaussian beam synthetics for the compressional waves modeled (Figures 5A and 5B).

In Figures 4C and 5C, the envelope amplitudes for the first arrival synthetics are shown for models 1 and 2. For both cases, the analytic signals are computed and from these the envelope amplitudes are obtained following the procedure of MATHENEY and NOWACK (1995). For the given first arrival, the peak of the envelope amplitude is then obtained. For each model, the squares represent the peak envelope amplitudes from the reflectivity modeling and the plus signs are from the Gaussian beam modeling. For all cases, a large Q_p value of 2000 was used to emphasize only the structural effects on the amplitudes. A gap in the amplitudes near the cross-over distance results from the picking algorithm that discards traces if there are overlapping arrivals, such as at the cross-over distance.

In Figure 4C, the refracted wave amplitudes for model 1 from the reflectivity modeling (squares) are slightly lower than the amplitudes from the Gaussian beam modeling (plus signs). Nonetheless, the overall shape of the curve is very similar for the two methods. For the refracted arrivals, the envelope amplitudes are lower after the cross-over distance, and then are constant or very slightly increasing resulting from wave interference.

The envelope amplitudes for model 2 are shown in Figure 5C, and again are very similar between the two approaches. However, the reflectivity amplitudes decay slightly more with increasing distance for the refracted arrivals. After the cross-over distance, the refracted amplitudes are higher than for the previous case since the diving waves are now more significant at shorter distance ranges resulting from the steeper gradient. The amplitudes of the refracted waves increase slightly with distance until a distance of about 180 km, and then begin to decrease as the diving wave begins to separate. For both models 1 and 2, the incorporation of attenuation into the models would have the effect of further decreasing the amplitude curves with distance.

The frequency content of a specific arrival is characterized by the signal's frequency spectrum. However, the signal must be windowed to avoid secondary arrivals which may overlap with the primary arrival. Several methods have been used to represent the average frequency content of a signal in terms of a single measure. These have included measures of pulse broadening (TONN, 1989), the peak or centroid of the signal spectrum (QUAN and HARRIS, 1997) and the pulse instantaneous frequency (MATHENEY and NOWACK, 1995). Here we use the pulse instantaneous frequency as a measure of a representative pulse frequency. An advantage of using the pulse instantaneous frequency is that it is a localized time-domain measurement. However, an averaging window is usually applied for stability. Also, a slight damping of the estimate has been applied when the envelope amplitude is low (MATHENEY and NOWACK, 1995). In our case, the instantaneous frequency estimates are taken at the peak of the envelope of the first arrival. A disadvantage of instantaneous frequency or other single measures of the frequency content is that it cannot easily separate the effects of overlapping signals. For this, a sonogram approach based on either the short-time Fourier transform or a continuous wavelet transform is required (DAUBECHIES, 1992).

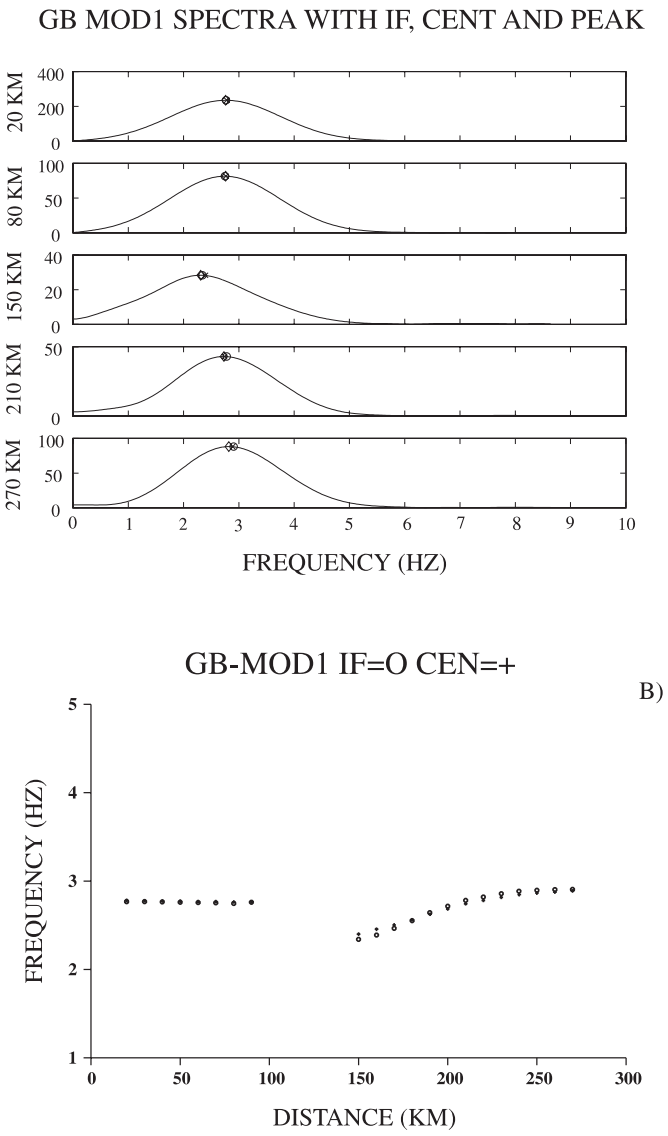

Figure 6
A) Spectra of first arrivals at several distances using Gaussian beam method showing the peak spectral amplitude (diamonds), the centroid frequency (crosses) and the instantaneous frequency (circles). B) Centroid frequencies (plus signs) and instantaneous frequencies (circles) are displayed for first arrivals with distance from Gaussian beam modeling.

Figure 4D shows the pulse instantaneous frequencies for model 1 obtained from the reflectivity calculations (squares) and the Gaussian beam method (plus signs). The gap in the estimates at the cross-over distance is where seismic attributes were

not computed because of crossing phases. The Gaussian beam estimates required large beam parameters for the wide-angle reflections in order to obtain the broadening effects of the refracted arrival after the cross-over distance for this model. Also, the instantaneous frequencies resulting from the reflectivity computations were found to be sensitive to the layer thickness used to approximate the gradient. For the comparison in Figure 4D, the double precision reflectivity algorithm of KIND (1978) was used with a reduced layer thickness of 0.1 km for the first 15 km below the interface.

At distances less than 100 km, the direct wave instantaneous frequencies are shown, and for distances greater than 125 km, the refracted wave instantaneous frequencies are shown. After the cross-over distance the instantaneous frequencies initially lower and then increase to values greater than those of the direct wave. This was initially surprising until an early description of this effect was found in ČERVENÝ and RAVINDRA (1971) for an asymptotic interference wave for a layer over a gradient. In their Figure 6.6, the spectra of the refracted waves are displayed at different distances. It shows that the peaks of the spectra initially lower after the critical distance compared to the incident pulse, then increase to values greater than the incident pulse, and finally lower to that of the incident wave after the separation of the diving wave. This is similar to the results for instantaneous frequencies found here for distances less than the separation of the diving wave.

To verify that the pulse instantaneous frequency estimates are representative of this frequency effect, the spectra of the first arrivals from the Gaussian beam modeling are shown in Figure 6A. In this figure, the crosses are the instantaneous frequencies, the circles are the centroid frequencies weighted by the power spectrum and the diamonds are the peaks of the spectra. In Figure 6B, a comparison of the weighted centroid frequencies and the pulse instantaneous frequencies at different distances are given, and the estimates are seen to compare reasonably well.

To understand why the instantaneous frequencies and the centroid frequencies are similar, the power theorem can be used (BRACEWELL, 1986), where

$$\int s_1(t)s_2^*(t)\,dt = \int s_1(\omega)s_2^*(\omega)\,\frac{d\omega}{2\pi} \quad .$$

If the analytic signal is written as $y(t) = a(t)e^{i\phi(t)}$, then $a(t)$ is the envelope amplitude, $\phi(t)$ is the instantaneous phase and $f(t) = d\phi/dt(t)$ is the instantaneous frequency, where the spectrum of the analytic signal is zero for negative frequencies. Letting $s_1(t) = dy(t)/dt = \dot{a}(t)e^{i\phi(t)} + if(t)y(t)$ with Fourier transform $s_1(\omega) = i\omega y(\omega)$, $s_2(t) = y(t)$ with Fourier transform $s_2(\omega) = y(\omega)$, and then equating imaginary parts in the power theorem above gives

$$\frac{\int f(t)a^2(t)\,dt}{\int a^2(t)\,dt} = \frac{\int \omega y^2(\omega)\,\frac{d\omega}{2\pi}}{\int y^2(\omega)\,\frac{d\omega}{2\pi}} \quad .$$

Thus, as the windowed average of the instantaneous frequency weighted by the squared envelope becomes larger, the estimate approaches the centroid of the power spectrum, where the frequency integrals are over the positive frequencies. For the example in Figure 6, the instantaneous frequencies are weighted over 11 points by the squared envelope. This suggests that the weighted instantaneous frequency is a useful local measure of the characteristic frequency of a signal, particularly if taken at the peak amplitude of a signal and with the averaging window chosen appropriately.

Figure 5D shows the instantaneous frequency estimates for the synthetic first arrivals obtained from model 2. This model has a steeper gradient than model 1 and results in the diving wave going to greater depths. As a result, the diving wave separates from the interference package at shorter distances as seen in Figures 5A and 5B. In Figure 5D, the plus symbols are for the Gaussian beam results and the squares are for the reflectivity results. The gap in the values at the cross-over distance is where attribute values were not estimated because of crossing phases. For distances exceeding the cross-over distance, the instantaneous frequency now initially increases to greater values than those of the direct wave, then slightly decreases and finally flattens with the separation of the diving wave.

The overall characteristics between the two synthetic results are similar, with the exception of the somewhat lower values of the pulse instantaneous frequencies for the reflectivity results just after the cross-over distance. This also occurred for model 1 when a larger layer thickness was used for the reflectivity modeling. As a result, the reflectivity results are slightly underestimated for this distance range. Nonetheless, the overall shape of the curves is similar between the two approaches and illustrates how the frequency characteristics of the refracted arrival change with distance out to the separation of the diving wave for this model.

Finally, models with interfaces and negative velocity gradients have been described by ČERVENÝ and RAVINDRA (1971) and result in diffracted head waves that have reduced amplitudes even compared to pure head waves. It has been suggested based on petrologic arguments that negative velocity gradients below the Moho should occur in many regions of high heat flow. However, this is contrary to the general observation that P_n arrivals are found worldwide. TITTGEMEYER *et al.* (1999) proposed that scattering from small-scale features superposed on negative velocity gradients can also generate P_n arrivals. It is as yet unclear if these small-scale features can be homogenized to larger scale, effective velocity and attenuation parameters for the modeling of wide-angle seismic data.

Conclusions

In this paper, several examples of refracted arrivals from simple layered models have been used to illustrate refraction effects of interfaces and velocity gradients on first arrival seismic attributes. The reflectivity and Gaussian beam methods have been used to compute synthetic seismograms, and from these seismic attributes obtained and compared. Using wide beam parameters for the reflected phases in the Gaussian beam method, and a small layer thickness for the reflectivity modeling, a good agreement was found for the seismic attributes obtained from the two methods. Thus, seismogram modeling can be used to simulate refraction effects on wide-angle seismic attributes. These effects can then be incorporated into the modeling and inversion for elastic and anelastic structure. The advantage of using the Gaussian beam method for the modeling of seismic attributes is that it is fast, and also asymptotically valid in laterally varying media.

Acknowledgements

The authors would like to acknowledge Prof. V. ČERVENÝ for his insightful work on ray and wave methods over the years. We also thank L. W. Braile, A. J. Rudman and M. Sen for providing reflectivity algorithms used in this paper.

REFERENCES

AKI, K. and RICHARDS, P. G., *Quantitative Seismology Theory and Methods* (W. H. Freeman and Co., San Francisco, 1980).

BRACEWELL, R. N., *The Fourier Transform and its Applications* (McGraw-Hill, New York, 1986).

BRAILE, L. W., *Interpretation of crustal velocity gradients and Q structure using amplitude-corrected seismic refraction profiles*. In *The Earth's Crust* (ed. J.G. Heacock) (Am. Geophys. Un. Monograph *20*, 1977), pp. 427–439.

BRAILE, L. W. and SMITH, R. B. (1975), *Guide to the Interpretation of Crustal Refraction Profiles*, Geophys. J.R. astr. Soc. *40*, 145–176.

ČERVENÝ, V., POPOV, M. M., and PŠENČÍK, I. (1982), *Computation of Wavefields in Inhomogeneous Media — Gaussian Beam Approach*, Geophys. J. R. astr. Soc. *70*, 109–128.

ČERVENÝ, V. (1985), *Gaussian Beam Synthetic Seismograms*, J. Geophys. *58*, 44–72.

ČERVENÝ, V. and RAVINDRA, R., *Theory of Seismic Head Waves* (University of Toronto Press, Toronto, 1971).

CHOY, G. L., CORMIER, V. F., KIND, R., MÜLLER, G., and RICHARDS, P. G. (1980), *A Comparison of Synthetic Seismograms of Core Phases Generated by the Full Wave Theory and by the Reflectivity Method*, Geophys. J. R. astr. Soc. *61*, 21–39.

CORMIER, V. F. and RICHARDS. P. G. (1977), *Full Wave Theory Applied to a Discontinuous Velocity Increase: The Inner Core Boundary*, J. Geophys. *43*, 3–31.

DAUBECHIES, I., *Ten Lectures on Wavelets* (SIAM, Philadelphia, 1992).

FUCHS, K. and MÜLLER, G. (1971), *Computation of Synthetic Seismograms with the Reflectivity Method and Comparison with Observations*, Geophys. J.R. astr. Soc. *23*, 417–433.

HILL, D. (1971), *Velocity Gradients and Anelasticity from Crustal Body-wave Amplitudes*, J. Geophys. Res. *76*, 3309–3325.

HILL, D. (1973), *Critically Refracted Waves in a Spherically Symmetric Radially Heterogeneous Earth Model*, Geophys. J.R. astr. Soc. *34*, 149–177.

KENNETT, R. L. N. and ENGDAHL, E. R. (1991), *Traveltimes for Global Earthquake Location and Phase Identification*, Geophys. J. Int. *105*, 429–465.

KIND R. (1978), *The Reflectivity Method for a Buried Source*, J. Geophys. *44*, 603–612.

MATHENEY, M. P. and NOWACK, R. L. (1995), *Seismic Attenuation Values Obtained from Instantaneous-frequency Matching and Spectral Ratios*, Geophys. J. Int. *123*, 1–15.

MATHENEY, M. P., NOWACK, R. L. and TREHU, A. M. (1997), *Seismic Attribute Inversion for Velocity and Attenuation Structure*, J. Geophys. Res. *102*, 9949–9960.

MÜLLER, G, 1985, *The Reflectivity Method: A Tutorial*, J. Geophys. *58*, 153–174.

NOWACK, R. L. (2002), *Calculation of Synthetic Seismograms with Gaussian Beams*, Pure appl. geophys., in press.

NOWACK, R. L. and AKI, K (1984), *The Two-dimensional Gaussian Beam Synthetic Method: Testing and Application*, J. Geophys. Res. *89*, 7797–7819.

NOWACK, R. L. and MATHENEY, M. P. (1997a), *Inversion of Seismic Attributes for Velocity and Attenuation Structure*, Geophys. J. Int. *128*, 689–700.

NOWACK, R. L. and MATHENEY, M. P. (1997b), *Extraction of Seismic Attributes from Wide-angle Synthetic Data Derived with Models with Interfaces*, Trans. Am. Geophys. Un. EOS *78*.

QUAN, Y. and HARRIS, J. M. (1997), *Seismic Attenuation Tomography Using the Frequency Shift Method*, Geophysics *62*, 895–905.

POPOV M. M. (1982), *A New Method of Computing Wavefields in the High-frequency Approximation*, Wave Motion *4*, 85–97.

RUDMAN, A. J., MALLICK, S., FRAZER, L. N., and BROMIRSKI, P. (1993), *Workstation Computation of Synthetic Seismograms for Vertical and Horizontal Profiles: A Full Wavefield Response for a Two-dimensional Layered Half-space*, Computers and Geosciences *19*, 447–474.

SERENO, T. J. and GIVEN, J. W. (1990), *P_n Attenuation for a Spherically Symmetric Earth Model*, Geophys. Res. Lett. *17*, 1141–1144.

TITTGEMEYER, M., WENZEL, F. and FUCHS, K. (1999), *On the Nature of P_n*, Am. Geophys. Un. EOS *80*, F711.

TONN, R. (1991), *Comparison of Seven Methods for the Computation of Q*, Phys. Earth Planet. Int. *55*, 259–268.

(Received September 29, 2000, revised March 3, 2001, accepted March 30, 2001)